Deblur Gaussian Splatting SLAM

Francesco Girlanda[1]   Denys Rozumnyi[1]   Marc Pollefeys[1,2]   Martin R. Oswald[3]

[1]ETH Zürich   [2]Microsoft   [3]University of Amsterdam

Figure 1. **Deblur-SLAM** can successfully track the camera and reconstruct sharp maps for highly motion-blurred sequences. We directly model motion blur, which enables us to achieve high-quality reconstructions, both on challenging synthetic (top) and real (bottom) data.

Abstract

We present Deblur-SLAM, a robust RGB SLAM pipeline designed to recover sharp reconstructions from motion-blurred inputs. The proposed method bridges the strengths of both frame-to-frame and frame-to-model approaches to model sub-frame camera trajectories that lead to high-fidelity reconstructions in motion-blurred settings. Moreover, our pipeline incorporates techniques such as online loop closure and global bundle adjustment to achieve a dense and precise global trajectory. We model the physical image formation process of motion-blurred images and minimize the error between the observed blurry images and rendered blurry images obtained by averaging sharp virtual sub-frame images. Additionally, by utilizing a monocular depth estimator along-side the online deformation of Gaussians, we ensure precise mapping and enhanced image deblurring. The proposed SLAM pipeline integrates all these components to improve the results. We achieve state-of-the-art results for sharp map estimation and sub-frame trajectory recovery both on synthetic and real-world blurry input data.

1. Introduction

The challenge of reconstructing the real world with high fidelity has long been a core problem in computer vision, essential for applications such as robotic navigation, VR/AR, architecture, and autonomous vehicles. Achieving accurate, detailed representations of physical environments is crucial, and dense visual Simultaneous Localization and Mapping (SLAM) systems address this by estimating a precise reconstruction of an environment while simultaneously localizing the camera frames.

Traditional 3D SLAM approaches typically rely on geometric representations, implemented in various forms, such as weights of an MLP [1, 39, 45, 63], features anchored in dense grids [5, 32, 44, 54, 64, 74, 75, 89, 90], hierarchical octrees [79] and points/surfels [27, 56, 68], mesh [3], and voxel hashing [8, 40, 49, 85, 86]. Recent visual SLAM approaches further capture visual appearance, drawing on advances in Neural Radiance Fields (NeRF) [42] and its variants [29, 43], allowing for photorealistic image synthesis of environments. These advances enable new possibilities in complex downstream tasks, including detailed semantic scene understanding [23], language-guided manipulation [59], and visual nav-

igation [58]. Additionally, neural representations have the advantage of filling unseen regions with smooth geometric estimation and offering a low-memory footprint [45, 63, 71].

Methods based on 3D Gaussian Splatting (3DGS) [29] yield high-fidelity renderings [22, 26, 41, 53, 76, 81] and show promising results in the RGB-only setting, given their flexibility in optimizing surface locations [22, 41, 53]. However, these methods often lack multi-view depth and geometric priors, leading to suboptimal geometry in RGB-only applications. Most approaches also only implement frame-to-model tracking without global trajectory and map optimization, which can result in excessive drift, especially under real-world conditions. Frame-to-frame tracking methods, combined with loop closure and global bundle adjustment (BA), still achieve state-of-the-art tracking accuracy [82, 84, 86]. The current state-of-the-art in SLAM is SplatSLAM [53], which seeks to incorporate the strengths of frame-to-frame methods by integrating loop closure, global bundle adjustment, and deformable 3D Gaussian maps.

At the same time, motion blur is a common phenomenon that degrades image quality due to fast camera motion – a common failure of most state-of-the-art SLAM and 3D reconstruction methods. These methods do not employ any strategy to handle severe motion-blurred images that usually lead to worse reconstruction quality.

The proposed Deblur-SLAM method aims to solve the under-constrained motion-blurred setting. It combines both frame-to-frame and frame-to-model approaches and estimates sub-frame trajectories that lead to sharper reconstructions (see Fig. 1). We make the following **contributions**:

- We propose an RGB SLAM method that explicitly addresses and models camera motion blur. This leads to sharp maps even when input frames are highly blurred by fast camera motion.
- For increased robustness, we combine frame-to-frame and frame-to-model trackers and, for the first time, incorporate loop closure, bundle adjustment, and online refinement into a deblurring SLAM framework.
- In contrast to most SLAM methods, we estimate trajectories with sub-frame precision.

2. Related work

Dense visual SLAM. Curless and Levoy [9] pioneered dense online 3D mapping using truncated signed distance functions (TSDF). KinectFusion [44] demonstrated real-time SLAM through depth maps. To address pose drift, globally consistent pose estimation and dense mapping techniques have been developed, often by dividing the global map into submaps [4, 6, 7, 11, 17, 20, 24, 25, 33, 36–38, 40, 48, 61, 67, 67]. Loop detection triggers submap deformation via pose graph optimization [6, 7, 15, 16, 19–21, 25, 30, 33, 37, 38, 40, 48, 56, 61, 67, 70, 77], and global bundle adjustment (BA) is employed for refine-

ment [6, 8, 11, 21, 40, 56, 67, 68, 77, 80]. While 3D Gaussian SLAM with RGB-D input has demonstrated promising results, these methods do not consider global consistency through mechanisms like loop closure [26, 81, 86]. Point-SLAM [52] creates photorealistic 3D maps using a dynamic neural point cloud. DROID-SLAM [68] achieves global consistency directly minimizing reprojection errors, which iteratively refines dense optical flow and camera poses. Recent advancements like GO-SLAM [86], HI-SLAM [85], and GlORIE-SLAM [82] optimize factor graphs for accurate tracking. For a recent in-depth survey on NeRF-inspired dense SLAM, we refer to [69].

RGB SLAM. Most research concentrates on combining RGB and depth cameras. RGB-only methods are less explored due to the lack of geometric data, which introduces scale, depth ambiguities, motion blur and motion parallax effects. Nonetheless, dense SLAM using only RGB cameras is attractive for its cost-effectiveness and versatility across different environments. MonoGS [41] and Photo-SLAM [22] were pioneers in implementing RGB-only SLAM using 3D Gaussians. However, their lack of proxy depth information limits their ability to achieve high-accuracy mapping. MonoGS [41] does not ensure global consistency either. SplatSLAM [53] incorporates global consistency but lacks strategies to handle motion blur as well as modeling dense sub-frame trajectories.

Image deblurring. Motion blur significantly impacts the output quality of many computer vision methods and has been a longstanding subject of active research. Various studies have addressed the effects of motion blur, enabling the reconstruction of sharp 3D maps when the input images are blurred [12, 13, 18, 31, 35, 57]. In visual SLAM systems, input measurements are particularly susceptible to motion blur because a moving camera captures images over the exposure period. To mitigate this, we parametrize the camera trajectory during the exposure time and optimize sub-frame camera poses to match the blurred inputs, similar to the approaches in [2, 50, 51, 72, 87, 88]. Similar to our setting, I^2-SLAM [2] aims to reconstruct photorealistic and sharp maps from casually captured videos that contain severe motion blur and varying appearances. In contrast to our work, it lacks global consistency through loop closure, bundle adjustment, an online refinement of the deformable 3D Gaussian map, and, specifically for the RGB setting, a monocular depth estimator to improve Gaussian initialization.

The proposed Deblur-SLAM overcomes these limitations by leveraging a globally consistent tracker, a monocular depth estimator, and a deformable 3D Gaussian map that adapts online to loop closure and global bundle adjustment, as in [53]. By directly modeling the camera motion blur, we present a complete pipeline that addresses blur, which is the most common issue of state-of-the-art SLAM methods.
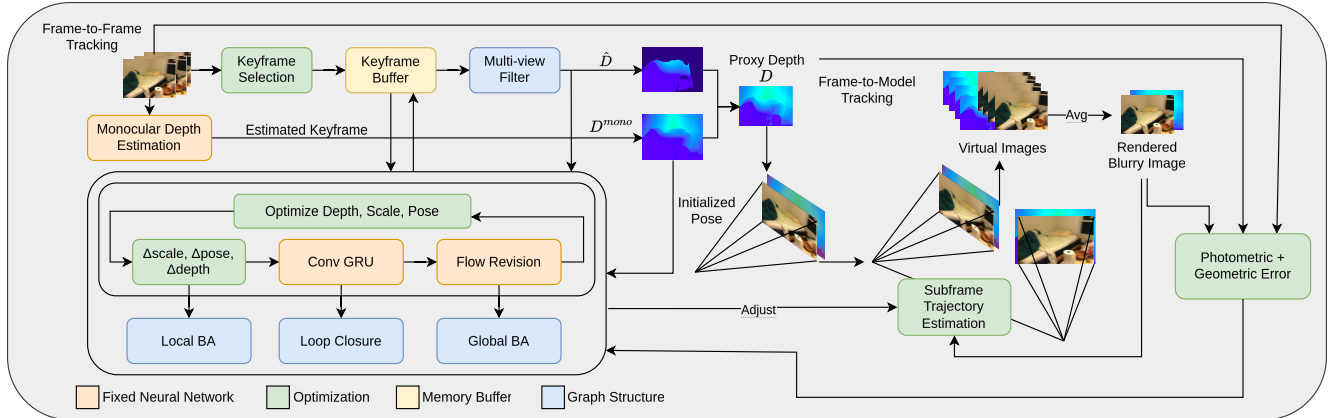
Figure 2. **Architecture of Deblur-SLAM.** Given an RGB input stream, we estimate an initial pose through local bundle adjustment (BA) using joint Disparity, Scale and Pose Optimization (DSPO). This pose is later refined through frame-to-model tracking that learns a sub-frame trajectory. Each keyframe is then mapped, taking advantage of the estimated monocular depth. The sub-frame trajectory is applied to render virtual sharp images, which model the physical image formation of blurry images. We optimize the photometric and geometric error between the observed blurry image and the average of our sharp images. We further refine poses globally via online loop closure, global BA, and a deformable 3D Gaussian map that adjusts for global pose and depth updates before each mapping phase.

3. Method

Deblur-SLAM aims to bridge the strengths of both frame-to-frame and frame-to-model approaches in order to get sub-frames trajectories that lead to sharp reconstructions in a motion-blurred setting. We leverage SplatSLAM [53]'s frame-to-frame features to provide precise initialization of both camera poses and Gaussians. Then, we stack a frame-to-model tracker on top to learn the sub-frame trajectory, allowing sharp images to be rendered at sub-frame precision. We refer to these sharp images as ‚virtual images', which can be used to generate a video with a higher frame rate. We optimize the photometric and geometric error between the observed blurry image and the synthesized blurred image, obtained by averaging the sharp virtual sub-frames (Fig. 2). During optimization, we use an adjustment process to regularize the sub-frame trajectory, aligning it with the global trajectory to achieve a highly accurate and detailed reconstruction. These three components – frame-to-frame tracker, frame-to-model tracker, and blur decomposition – are the main components of the proposed method, which are detailed in the following subsections.

3.1. Motion blur image formation model

The physical formation process of an image in a digital camera consists of gathering photons during the exposure period that are later converted to a digital image. This process can be formalized by integrating a sequence of sharp images:

$$B(u) = \phi \int_0^\tau C_t(u)dt \ , \qquad (1)$$

where $B(u) \in \mathbb{R}^3$ represents the motion-blurred image, $u \in \mathbb{R}^2$ is a pixel in the image, ϕ is a normalization factor, τ

is the exposure time, $C_t(u) \in \mathbb{R}^3$ is the virtual sharp image captured at sub-frame time $t \in [0, \tau]$. This camera model approximates motion blur by discretizing into M timestamps (or virtual views):

$$B(u) \approx \frac{1}{M} \sum_{i=0}^{M-1} C_i(u) \ . \qquad (2)$$

The camera trajectory representation is parametric and has a fixed number of control points (by default, we use 2). We use M virtual cameras/views that are obtained through a linear interpolation between the control points using LERP (Linear intERPolation) for the translation vector and SLERP (Spherical Linear intERPolation) for the rotation matrix. By rendering views from the virtual cameras, we obtain so-called virtual sharp images. The pipeline can be easily extended to more complex interpolations, such as the cubic B-spline interpolation with four control points in the **SE(3)** space. We refer to prior work [34, 72, 87] for details about the interpolation and derivations of the related Jacobian.

3.2. Deformable 3D Gaussian Splatting

We adopt a deformable 3D Gaussian Splatting representation that allows us to achieve global consistency. The scene is represented by a set $\mathcal{G} = \{g_i\}_{i=1}^N$ of N 3D Gaussians. Each Gaussian g_i is parameterized by its centroid $\mu_i \in \mathbb{R}^3$, 3D covariance $\Sigma \in \mathbb{R}^{3 \times 3}$, opacity $\sigma \in [0, 1]$ and color $c \in \mathbb{R}^3$. The distribution of each scaled Gaussian is defined as:

$$g_i(\mathbf{x}) = \exp\left(-\frac{1}{2}\left(\mathbf{x} - \boldsymbol{\mu}_i\right)^\top \Sigma_i^{-1}\left(\mathbf{x} - \boldsymbol{\mu}_i\right)\right) \ . \qquad (3)$$

As in previous methods, we ensure that the 3D covariance Σ remains positive semi-definite. To reduce the optimization
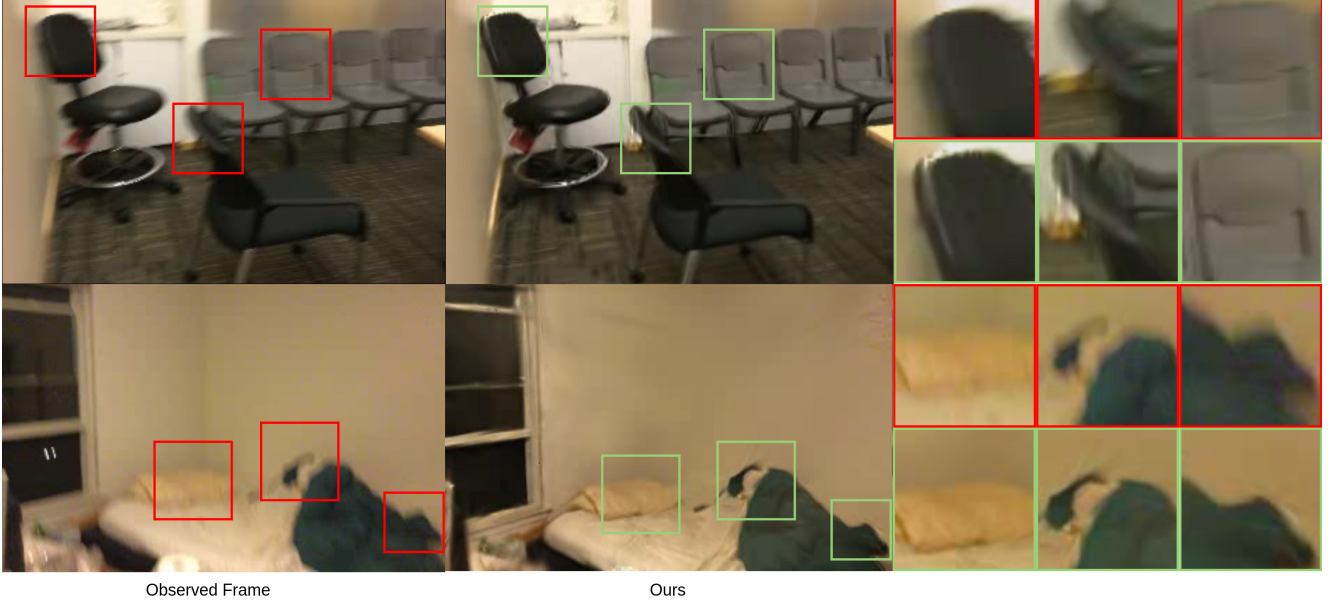
Observed Frame   Ours

Figure 3. **Qualitative results on real-world ScanNet [10] data.** Given the input blurry frames from scenes 0169 and 0207, we manage to track the trajectory with sub-frame precision and estimate sharp maps by directly modeling the camera motion blur.

complexity, 3DGS represents Σ_i using a scale $S_i \in \mathbb{R}^3$ and rotation matrix $R_i \in \mathbb{R}^{3\times3}$ stored by a quaternion $q_i \in \mathbb{R}^4$ leading to the decomposition $\Sigma_i = R_i S_i S_i^T R_i^T$.

Rendering. To render 3D Gaussians to a 2D plane, we project the covariance matrix Σ as $\Sigma' = JR\Sigma R^T J^T$ and project μ as $\mu' = K\omega^{-1}\mu$, where R is the rotation component of world-to-camera extrinsic ω^{-1}, and J is the Jacobian of the affine approximation of the projective transformation [91]. The final pixel color C and depth D^r at pixel x' is rendered by rasterizing the obtained Gaussians that overlap with the given pixel, sorted by their depth as

$$C = \sum_{i \in \mathcal{N}} \mathbf{c}_i \alpha_i \prod_{j=1}^{i-1}(1-\alpha_j) , \quad D^r = \sum_{i \in \mathcal{N}} \hat{d}_i \alpha_i \prod_{j=1}^{i-1}(1-\alpha_j) \tag{4}$$

where $\hat{d}_i$ is the z-axis depth of the center of the i-th Gaussian. We obtain the 2D opacity α_i by multiplying the 3D opacity o_i and the 2D Gaussian density as

$$\alpha_i = o_i \exp\left(-\frac{1}{2}\left(\mathbf{x}' - \boldsymbol{\mu}_i'\right)^\top \Sigma_i'^{-1}\left(\mathbf{x}' - \boldsymbol{\mu}_i'\right)\right) . \tag{5}$$

Map initialization. We assume the camera remains static for at least one initial frame at the start of the sequence. This approach ensures a sharp frame at the beginning of our pipeline, providing a reliable basis for effectively initializing the Gaussians. This assumption is common in real-life use cases and hold true for all tested real-world datasets. To improve the map initialization in the RGB setting, we make use of a proxy depth map D that combines the inlier multi-

view depth $\tilde{D}$ and the monocular depth D^{mono}:

$$D(u,v) = \begin{cases} \tilde{D}(u,v) & \text{if } \tilde{D}(u,v) \text{ is valid} \\ \theta D^{\text{mono}}(u,v) + \gamma & \text{otherwise} \end{cases}, \tag{6}$$

where θ and γ are computed as in the initial least square fitting (see supplementary material).

Keyframe selection. We employ the strategies from [41, 53], *i.e.* we use both an optical flow threshold τ_f and a keyframe selection strategy to avoid mapping redundant frames. Since our viewpoints now consist of interpolating two control points, we calculate the intersection over union (IoU) on the viewpoint using the midpoint between them.

Mapping loss. The rendered blurry image B_k is defined as:

$$B_k = a_k \left(\frac{1}{M}\sum_{i=0}^{M-1} C_i\right) + b_k , \tag{7}$$

where a_k and b_k are optimizable parameters to account for varying exposure and lightning changes, and M is the number of virtual images.

We optimize the difference between B_k and the observed input image, applying a photometric and geometric loss to the image and a scale regularizer to avoid artifacts from elongated Gaussians. Our photometric loss is defined as:

$$\mathcal{L}_{\text{ph}} = \lambda_{\text{SSIM}}\mathcal{L}_{\text{SSIM}} + (1 - \lambda_{\text{SSIM}})\left|B_k - B_k^{gt}\right|_1 , \tag{8}$$

where B_k is the image after the exposure correction of equation (7). This term, together with the geometric loss and the
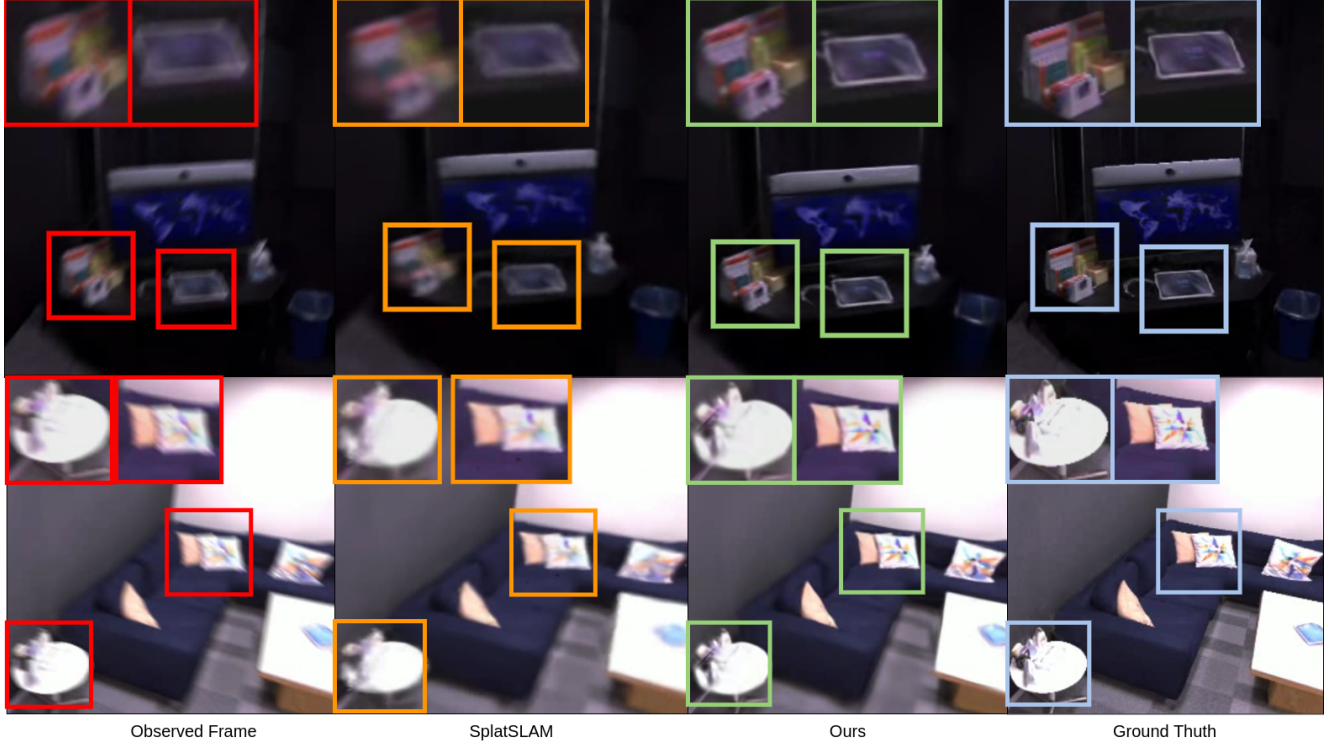
Figure 4. **Qualitative comparison to Splat-SLAM.** We compare in both a darker scene (office 1 – top) and a very bright scene (office 2 – bottom) on the newly proposed synthetically blurred Replica dataset [60], showing the versatility of the proposed model. From left to right: the observed frame with visible camera motion blur, the SplatSLAM [53] rendering, one of our sharp virtual images, and the ground truth. The proposed Deblur-SLAM method can recover more details such as the boxes (top) and the pillow (bottom).

scale regularizer, leads to the final optimization objective:

$$\min_{\mathcal{G},\mathbf{a},\mathbf{b}} \sum_{k \in \mathrm{KFs}} \frac{\lambda}{N_k} \mathcal{L}_{\mathrm{ph}} + \frac{1-\lambda}{N_k} \left| \bar{D}_k^r - D_k \right|_1 + \frac{\lambda_{\mathrm{reg}}}{|\mathcal{G}|} \sum_i^{|\mathcal{G}|} |s_i - \tilde{s}_i|_1 \,, \tag{9}$$

where KFs contains the set of keyframes in the local window, N_k is the number of pixels per keyframe, $\bar{D}_k^r$ is the average depth of the virtual views at frame k. We denote hyperparameters as λ, λ_{SSIM} and λ_{reg}. The mean scaling is represented by $\tilde{s}$. After the end of the online process, we perform a set of final refinements as in [41, 53, 82].

Map deformation. Since we update keyframe poses and proxy depth maps online, the 3D Gaussian map is adjusted by a non-rigid deformation as in [53]. We update the mean, scale, and rotation of all Gaussians g_i that are associated with the given keyframe. The mean μ_i is projected into ω to find pixel correspondence (u, v). Since the Gaussians are not necessarily anchored on the surface, instead of re-anchoring the mean at multi-view depth D', we shift the mean by $D'(u, v) - D(u, v)$ along the optical axis and update R_i and

s_i accordingly as

$$\boldsymbol{\mu}_i' = \left(1 + \frac{D'(u,v) - D(u,v)}{(\omega^{-1}\boldsymbol{\mu}_i)_z}\right) \omega' \omega^{-1} \boldsymbol{\mu}_i \,, \tag{10}$$

$$R_i' = R' R^{-1} R_i, s_i' = \left(1 + \frac{D'(u,v) - D(u,v)}{(\omega^{-1}\boldsymbol{\mu}_i)_z}\right) s_i \,. \tag{11}$$

3.3. Frame-to-frame tracking

In the tracking phase, we initialize the pose using a pre-trained recurrent optical flow model coupled with a Disparity, Scale and Pose Optimization (DSPO) objective from [53, 68], to optimize camera poses jointly with per-pixel disparities.

The optimization process uses the Gauss-Newton algorithm on a factor graph $G(V, E)$, where the nodes V represent the keyframe poses and disparities, and edges E model the optical flow between these keyframes. Odometry keyframe edges are incorporated into G by calculating the optical flow relative to the previously added keyframe. If the mean flow exceeds a threshold $\tau_f \in \mathbb{R}$, a new keyframe is introduced into G. The DSPO objective contains two distinct optimization objectives that are addressed in an alternating fashion. The primary objective, known as Dense Bundle Adjustment (DBA) [66, 68], jointly optimizes the

pose and disparity of the keyframes, as shown in equation (12). This objective operates on a sliding temporal window centered around the current frame, *i.e.*

$$\underset{\omega,d}{\arg\min} \sum_{(i,j)\in E} \left\| \tilde{p}_{ij} - K\omega_j^{-1} \left(\omega_i \left(1/d_i\right) K^{-1}[p_i, 1]^T \right) \right\|_{\Sigma_{ij}}^2 ,$$
(12)

where $\tilde{p}_{ij} \in \mathbb{R}^{(W\times H\times 2)\times 1}$ represents the predicted pixel coordinates after warping p_i into keyframe j via optical flow. Matrix K denotes the camera intrinsics, while ω_j and ω_i denote camera-to-world extrinsics. The Mahalanobis distance $\|\cdot\|_{\Sigma_{ij}}$ incorporates confidence-based weights.

The second objective, called Disparity, Scale and Pose Optimization (DSPO), refines disparity using monocular depth D^{mono} from a pretrained DPT model [46, 47], ensuring correct scale and shift estimation:

$$\underset{d^h,\theta,\gamma}{\arg\min} \sum_{(i,j)\in E} \left\| \tilde{p}_{ij} - K\omega_j^{-1} \left(\omega_i \left(1/d_i^h\right) K^{-1}[p_i, 1]^T \right) \right\|_{\Sigma_{ij}}^2$$
$$+ \alpha_1 \sum_{i\in V} \left\| d_i^h - \left(\theta_i \left(1/D_i^{\mathrm{mono}}\right) + \gamma_i\right) \right\|^2$$
(13)
$$+ \alpha_2 \sum_{i\in V} \left\| d_i^l - \left(\theta_i \left(1/D_i^{\mathrm{mono}}\right) + \gamma_i\right) \right\|^2 .$$

Here, the optimizable parameters are scales $\theta \in \mathbb{R}$, shifts $\gamma \in \mathbb{R}$ and a subset of disparities d^h classified as being high error (see supplementary material). This approach is used as the monocular depth is only valuable in regions where the multi-view disparity d_i optimization lacks accuracy. Additionally, setting $\alpha_1 < \alpha_2$ ensures that scales θ and shifts γ are optimized with the preserved low-error disparities d^l. The scale θ_i and shift γ_i are initially estimated using least squares fitting (see supplementary material). By optimizing DBA and DSPO alternatingly, we avoid the scale ambiguity encountered if d, θ, γ, and ω are optimized jointly.

Loop closure. To reduce scale and pose drift, we incorporate loop closure and online global bundle adjustment (BA) alongside local window frame tracking. As in [53], loop detection is performed by calculating the mean optical flow magnitude between the currently active keyframes within the local window and all previous keyframes. For each keyframe pair, we assess that the optical flow must be below a specified threshold τ_{loop}, and that the time interval between frames must exceed a set threshold τ_t ensuring co-visibility between the views. When both criteria are satisfied, a unidirectional edge is introduced into the graph.

Global BA. For the online global bundle adjustment (BA), a separate graph is constructed to include all keyframes up to the current point. Edges in this graph are added on the basis of the temporal and spatial relationships between keyframes. To ensure numerical stability, the scales of the disparities and poses are normalized before each global BA optimization.
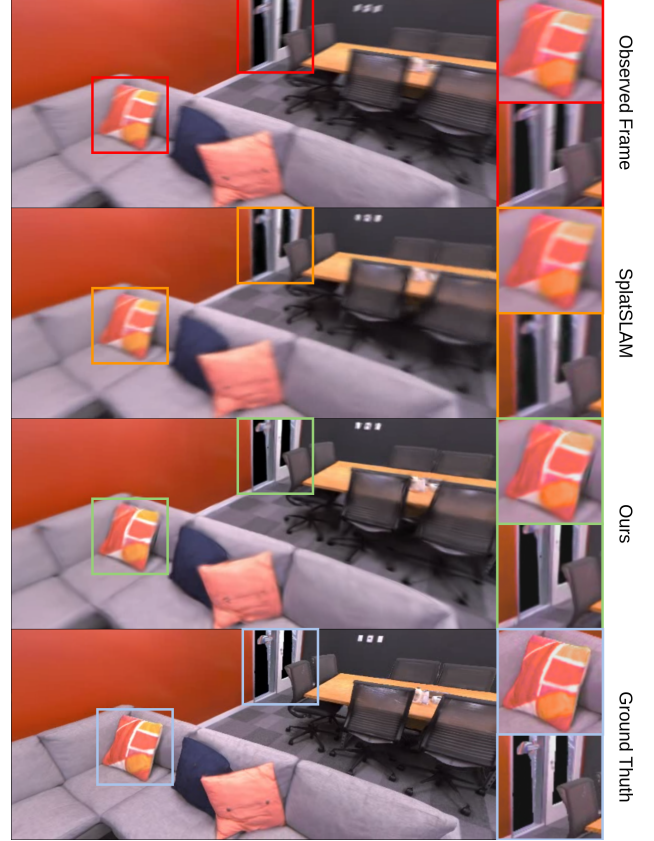

Figure 5. **Qualitative results on the Replica dataset (office 3 scene) [60].** We outperform Splat-SLAM [53] on blurry data.

3.4. Frame-to-model tracking

In contrast to Splat-SLAM [53], we further refine the previous frame-to-frame tracking by frame-to-model tracking using our deblur image formation model. Using the frame-to-frame pose as the initial pose (treated as a pose in the middle of the sub-frame trajectory), we run iterative optimization on the pose and affine brightness parameters for varying exposure. This initialization helps us to align with the global trajectory, which is estimated by the DSPO objective. This step also allows us to minimize the difference between the average of generated sharp virtual subframes and the observed blurry image. The optimization objective is as follows:

$$\mathcal{L}_1 = \frac{1}{N} \sum_{i=1}^{N} \left(\overline{\alpha}(i) \cdot \left| B(i) \cdot W(i) - B_{\mathrm{gt}}(i) \cdot W(i) \right| \right) , \quad (14)$$

where $\overline{\alpha}$ represents the mean of opacities that allows us to mask the yet unmapped part of the input image. Then, W is an edge mask used to calculate the gradient only on the edge pixel, $B(i)$ is a pixel of the image after the exposure correction as defined in (7), and B_{gt} is the blurry observed image. N is the number of pixels. Frame index k is omitted

Method	Metric	office0	office1	office2	office3	office4	room0	room1	room2	Avg.	Avg. w.o. ✗
MonoGS [41]	sPSNR↑	25.30	27.82	21.81	23.91	23.61	22.21	20.95	24.95	23.82	24.11
	sSSIM↑	0.82	**0.88**	0.81	0.83	0.85	0.72	0.74	0.82	0.81	0.82
	sLPIPS↓	0.43	0.30	0.40	0.32	0.40	0.47	0.48	0.37	0.40	0.39
	sATE[cm]↓	30.84	13.97	50.16	3.69	108.62	44.05	51.80	11.51	39.33	41.89
Splat-SLAM [53]	sPSNR↑	28.52	28.88	22.53	25.01	25.25	23.71	✗	✗	✗	25.65
	sSSIM↑	0.84	0.87	0.79	0.81	0.84	0.74	✗	✗	✗	0.82
	sLPIPS↓	0.36	0.30	0.35	0.27	0.34	0.39	✗	✗	✗	0.34
	sATE[cm]↓	**2.88**	**2.12**	2.34	2.05	4.53	1.90	✗	✗	✗	2.64
Deblur-SLAM (Ours)	sPSNR↑	30.40	30.29	25.20	26.52	27.06	25.75	25.25	27.74	27.28	27.54
	sSSIM↑	0.87	0.88	0.84	0.87	0.86	0.80	0.76	0.85	0.84	0.85
	sLPIPS↓	0.24	0.21	0.27	0.16	0.25	0.23	0.34	0.22	0.24	0.23
	sATE[cm]↓	3.04	2.94	1.52	1.00	3.75	1.08	5.87	3.78	2.87	2.22

Table 1. **Sub-frame evaluation on Replica [60].** Since this is a synthetic dataset, ground truth sub-frame trajectories and renderings are available. Thus, we evaluate the sub-frame version of PSNR, SSIM, LPIPS, and ATE (denoted by "s" in front). Our method achieves new state-of-the-art performance in estimating those sub-frame trajectories and renderings. A complete failure of the method is denoted by ✗. The best-performing method is denoted by bold font and dark green color, second best by light green, and worst-performing by yellow.

for simplicity.

While tracking further frames, we take advantage of the frame-to-frame online optimization and adjust the sub-frame trajectories using linear interpolation to follow the learned global trajectory.

Exposure gap estimation. In the above optimization, we further introduce two parameters to model the exposure gap between input frames. This helps improving the rendering quality on real-world datasets. We learn these two parameters by rendering each keyframe's previous and next frames following the same procedure used for the frame-to-model step. In addition, we include a regularization term to ensure that the learned subframe trajectory remains smooth. Concretely, we minimize the distance between the end of the previous frame and the beginning of the current keyframe, taking the gap parameter into account. The same approach is applied between the current keyframe and the next frame.

To achieve this, we compute two interpolation points, one between the previous and the current frame, as well as one between the current and the next frame:

$$t_{\text{prev}} = 0.5 + g_{\text{prev}}, \quad t_{\text{next}} = 0.5 + g_{\text{next}}, \quad (15)$$

which indicates how far along the motion is between the midpoint extrinsics of the respective frames. $g_{\text{prev}}, g_{\text{next}}$ represent the exposure gaps. We use linear interpolation for the translation components and SLERP for the quaternions to obtain the expected start and end pose. We then compare this interpolated pose with the actual viewpoint pose by measuring the squared norm of their translational difference and the squared quaternion angle difference of their rotations:

$$\mathcal{L}_{\text{trans}} = \left\| \mathbf{t}_{\text{viewpoint}} - \mathbf{t}_{\text{interp}} \right\|^2, \quad (16)$$

$$\mathcal{L}_{\text{rot}} = \left\| 2 \arccos\left(\left| \mathbf{q}_1^{-1} \cdot \mathbf{q}_2 \right| \right) \right\|^2. \quad (17)$$

where $\mathcal{L}_{\text{trans}}$ is the squared norm of the difference between the translation vectors, and $\mathcal{L}_{\text{rot}}$ is the squared norm of the angular difference between the two quaternions corresponding to the rotation matrices.

4. Experiments

Datasets. To evaluate our method, we generate a synthetically blurred Replica dataset made from the scenes used in [41]. By linearly interpolating the existing trajectory we added 8 sub-poses in between the existing ones. We rendered the new frames using Habitat-Sim [65] and then averaged 36 frames to create a blurry dataset for evaluation. We also test on real-world data using the TUM-RGBD [62], ScanNet datasets [10] and ETH3D [55] datasets.

Metrics. For evaluation on Replica [60], we report PSNR, SSIM [73] and LPIPS [83] on the rendered keyframe images against the original sharp images (denoted by "s" in front as in Table 1). Thus, we also evaluate the deblurring capabilities. For evaluation on ScanNet and TUM-RGBD, we evaluate the Absolute Trajectory Error (ATE) [62] between the virtual camera poses (as interpolated between two control points) and the ground truth poses used to render the dataset in Replica. For real-world datasets, we evaluate the mid-pose of the two control points against the ground truth.

Implementation details. We use 9 virtual cameras for the synthetic Replica dataset (as we use the original one and the 8 generated ones) to maintain a good correspondence with the original data while taking advantage of the fact that 9 is a divisor of the 36 averaged frames. We use 5 virtual cameras for the real-world data (but compare only to a single ground truth pose as sub-frame ground truth is unavailable). We keep the same frame-to-frame parameters as in [53]. Experiments are conducted on an AMD EPYC 7742 processor and NVIDIA GPU GeForce RTX 3090 with 24 GB memory.

Results on synthetic data. We tested our method on the proposed synthetic Replica dataset with sub-frame ground truth. Qualitative results are in Figs. 4 and 5. These results show that our method successfully models the physical blur formation and renders sharp virtual images. Our method outperforms all other methods on all metrics (Table 1).

Method	Metric	0000	0059	0106	0169	0181	0207	**Avg.**
MonoGS [41]	ATE [cm]↓	149.2	96.8	155.5	140.3	92.6	101.9	122.7
Splat-SLAM [53]	ATE [cm]↓	**5.5**	9.1	**7.0**	8.2	8.3	7.5	7.6
Deblur-SLAM (Ours)	ATE [cm]↓	6.1	**8.9**	7.4	**8.0**	**7.4**	**7.3**	**7.5**

Table 2. **Trajectory evaluation on ScanNet [10].** We achieve state-of-the-art results on trajectory estimation. We refer to qualitative results on this dataset (Fig. 3) to highlight the deblurring capabilities of Deblur-SLAM.

Method	Method	f1/desk	f2/xyz	f3/off	f1/desk2	f1/room	**Avg.**
MonoGS [41]	ATE [cm]↓	3.8	5.2	2.9	75.7	76.6	32.84
Splat-SLAM [53]	ATE [cm]↓	**1.6**	**0.2**	**1.4**	2.8	**4.2**	2.04
Deblur-SLAM (Ours)	ATE [cm]↓	**1.6**	**0.2**	1.5	**2.5**	**4.2**	**2.00**

Table 3. **Trajectory evaluation on TUM-RGBD [62].** As in Table 2, we evaluate the tracking performances of our method. Our method yields similar or better tracking errors than Splat-SLAM and strongly outperforms MonoGS.

Method	Metric	f1/desk	f2/xyz	f3/off	**Avg.**
I^2-SLAM [2]	ATE [cm]↓	**1.6**	0.3	1.9	1.3
Deblur-SLAM	ATE [cm]↓	**1.6**	**0.2**	**1.5**	**1.1**

Table 4. **Tracking performances on TUM-RGBD [62],** compared to the only related method that solves a similar problem. Our method achieves more accurate trajectory estimates (other properties cannot be evaluated since their code is not publicly released).

Method	Metric	sofa 1	sfm_bench	plant_scene_1
SplatSLAM [53]	PSNR↑	20.50	15.44	**28.42**
	SSIM↑	0.66	0.46	**0.87**
	LPIPS↓	0.43	0.56	0.18
	sPSNR↑	14.09	12.07	21.74
	sSSIM↑	0.53	0.39	0.77
	sLPIPS↓	0.61	0.65	0.28
Deblur-SLAM (Ours)	PSNR↑	**26.60**	**19.96**	28.38
	SSIM↑	**0.89**	**0.71**	**0.87**
	LPIPS↓	**0.18**	**0.35**	**0.14**
	sPSNR↑	**15.00**	**13.72**	**23.00**
	sSSIM↑	**0.62**	**0.55**	**0.81**
	sLPIPS↓	**0.56**	**0.51**	**0.22**

Table 5. **Rendering evaluation on ETH3D [55]** with synthetically blurred frames. By averaging frames to introduce blur we can evaluate method performance against GT. Our method outperforms Splat-SLAM on both sharp (denoted with "s" prefix) and averaged rendering metrics.

Results on real data. In real-world datasets, the absence of proper ground truth prevents testing the sharp frames directly. A recent method solving a similar problem has been introduced in I^2-SLAM [2], but sharp frames are manually selected, and metrics are evaluated solely on these frames, potentially introducing bias. To date, there is no available information about the specific frames used, nor has the code been shared, making comparisons challenging. Only trajectory evaluation on TUM-RGBD could be compared, shown in Table 4. Our method outperforms I^2-SLAM in this setting. Additionally, we present evaluation on ScanNet and TUM-RGBD datasets in Tables 2 and 3, evaluating the trajectory error against other baselines. Our method outperforms all other methods on trajectory error (ATE).

Test on Blurry Real-World Dataset. To further assess our model, we conducted experiments on the TUM-RGBD dataset [62] and ETH3D [55], where we increased the motion blur by averaging 2-5 frames. We matched the number of virtual cameras to the number of averaged frames, allowing us to pair each virtual image with a high-quality ground-truth frame. This setup enables us to showcase the effectiveness of our method in a different scenario. We managed to surpass all other metrics, demonstrating the overall effectiveness of our approach. We achieve better outcomes, especially for sharp virtual images, and observe a significant improvement in the ATE. The results can be seen in Table 5. More experiments and qualitative results can be found in the supplementary material.

Runtime. We tested the runtime of our method on ScanNet scene 0106_00, where it is 0.36 fps. Consequently, in terms of virtual sub-frame images, the runtime is 1.82 fps. This evaluation includes only the online process and not the final offline refinement at the end.

Limitations. Our method does not model and recover motion blur from moving objects. This requires further decomposition and is an interesting future work. In practice, not all video frames are blurry, and the high computational overhead for deblurring could be reduced by dynamically adapting the generated number M of virtual views.

5. Conclusions

We presented Deblur-SLAM, a robust RGB SLAM pipeline to recover sharp reconstructions from blurry inputs. Our pipeline takes advantage of sub-frame trajectory modeling, online loop closure, and global BA to achieve dense and accurate trajectories. Moreover, we model the physical image formation process of motion-blurred images and ensure sharp, sub-frame, and precise mapping thanks to the monocular depth estimator and online deformation of Gaussians. Deblur-SLAM applies these techniques in the context of scene deblurring for the first time. Experiments show that our method outperforms existing methods.

References

[1] Dejan Azinović, Ricardo Martin-Brualla, Dan B Goldman, Matthias Nießner, and Justus Thies. Neural rgb-d surface reconstruction. In *IEEE/CVF Conference on Computer Vision and Pattern Recognition*, pages 6290–6301, 2022. 1

[2] Gwangtak Bae, Changwoon Choi, Hyeongjun Heo, Sang Min Kim, and Young Min Kim. I2-slam: Inverting imaging process for robust photorealistic dense slam. *arXiv preprint arXiv:2407.11347*, 2024. 2, 8

[3] Michael Bloesch, Tristan Laidlow, Ronald Clark, Stefan Leutenegger, and Andrew J Davison. Learning meshes for dense visual slam. In *Proceedings of the IEEE/CVF International Conference on Computer Vision*, pages 5855–5864, 2019. 1

[4] Michael Bosse, Paul Newman, John Leonard, Martin Soika, Wendelin Feiten, and Seth Teller. An atlas framework for scalable mapping. In *2003 IEEE International Conference on Robotics and Automation (Cat. No. 03CH37422)*, pages 1899–1906. IEEE, 2003. 2

[5] Aljaž Božič, Pablo Palafox, Justus Thies, Angela Dai, and Matthias Nießner. Transformerfusion: Monocular rgb scene reconstruction using transformers. *arXiv preprint arXiv:2107.02191*, 2021. 1

[6] Yan-Pei Cao, Leif Kobbelt, and Shi-Min Hu. Real-time high-accuracy three-dimensional reconstruction with consumer rgb-d cameras. *ACM Transactions on Graphics (TOG)*, 37(5): 1–16, 2018. 2

[7] Sungjoon Choi, Qian-Yi Zhou, and Vladlen Koltun. Robust reconstruction of indoor scenes. In *IEEE Conference on Computer Vision and Pattern Recognition*, pages 5556–5565, 2015. 2

[8] Chi-Ming Chung, Yang-Che Tseng, Ya-Ching Hsu, Xiang-Qian Shi, Yun-Hung Hua, Jia-Fong Yeh, Wen-Chin Chen, Yi-Ting Chen, and Winston H Hsu. Orbeez-slam: A real-time monocular visual slam with orb features and nerf-realized mapping. *arXiv preprint arXiv:2209.13274*, 2022. 1, 2

[9] Brian Curless and Marc Levoy. Volumetric method for building complex models from range images. In *SIGGRAPH Conference on Computer Graphics*. ACM, 1996. 2

[10] Angela Dai, Angel X. Chang, Manolis Savva, Maciej Halber, Thomas Funkhouser, and Matthias Nießner. ScanNet: Richly-annotated 3D reconstructions of indoor scenes. In *Conference on Computer Vision and Pattern Recognition (CVPR)*. IEEE/CVF, 2017. 4, 7, 8, 13, 15

[11] Angela Dai, Matthias Nießner, Michael Zollhöfer, Shahram Izadi, and Christian Theobalt. Bundlefusion: Real-time globally consistent 3d reconstruction using on-the-fly surface reintegration. *ACM Transactions on Graphics (ToG)*, 36(4):1, 2017. 2

[12] Peng Dai, Yinda Zhang, Xin Yu, Xiaoyang Lyu, and Xiaojuan Qi. Hybrid neural rendering for large-scale scenes with motion blur. In *Proceedings of the IEEE/CVF Conference on Computer Vision and Pattern Recognition*, pages 154–164, 2023. 2

[13] François Darmon, Lorenzo Porzi, Samuel Rota-Bulò, and Peter Kontschieder. Robust gaussian splatting. *arXiv preprint arXiv:2404.04211*, 2024. 2

[14] Ainaz Eftekhar, Alexander Sax, Jitendra Malik, and Amir Zamir. Omnidata: A scalable pipeline for making multi-task mid-level vision datasets from 3d scans. In *Proceedings of the IEEE/CVF International Conference on Computer Vision*, pages 10786–10796, 2021. 13

[15] Felix Endres, Jürgen Hess, Nikolas Engelhard, Jürgen Sturm, Daniel Cremers, and Wolfram Burgard. An evaluation of the rgb-d slam system. In *2012 IEEE international conference on robotics and automation*, pages 1691–1696. IEEE, 2012. 2

[16] Jakob Engel, Thomas Schöps, and Daniel Cremers. Lsd-slam: Large-scale direct monocular slam. In *European conference on computer vision*, pages 834–849. Springer, 2014. 2

[17] Nicola Fioraio, Jonathan Taylor, Andrew Fitzgibbon, Luigi Di Stefano, and Shahram Izadi. Large-scale and drift-free surface reconstruction using online subvolume registration. In *Proceedings of the IEEE Conference on Computer Vision and Pattern Recognition*, pages 4475–4483, 2015. 2

[18] Jiandong Guo, Rongrong Ni, and Yao Zhao. Deblurslam: A novel visual slam system robust in blurring scene. In *2021 IEEE 7th International Conference on Virtual Reality (ICVR)*, pages 62–68, 2021. 2

[19] Peter Henry, Michael Krainin, Evan Herbst, Xiaofeng Ren, and Dieter Fox. Rgb-d mapping: Using kinect-style depth cameras for dense 3d modeling of indoor environments. *The international journal of Robotics Research*, 31(5):647–663, 2012. 2

[20] Peter Henry, Dieter Fox, Achintya Bhowmik, and Rajiv Mongia. Patch volumes: Segmentation-based consistent mapping with rgb-d cameras. In *2013 International Conference on 3D Vision-3DV 2013*, pages 398–405. IEEE, 2013. 2

[21] Jiarui Hu, Mao Mao, Hujun Bao, Guofeng Zhang, and Zhaopeng Cui. CP-SLAM: Collaborative neural point-based SLAM system. In *Thirty-seventh Conference on Neural Information Processing Systems*, 2023. 2

[22] Huajian Huang, Longwei Li, Hui Cheng, and Sai-Kit Yeung. Photo-slam: Real-time simultaneous localization and photorealistic mapping for monocular, stereo, and rgb-d cameras. *arXiv preprint arXiv:2311.16728*, 2023. 2

[23] Krishna Murthy Jatavallabhula, Alihusein Kuwajerwala, Qiao Gu, Mohd Omama, Tao Chen, Alaa Maalouf, Shuang Li, Ganesh Iyer, Soroush Saryazdi, Nikhil Keetha, Ayush Tewari, Joshua B. Tenenbaum, Celso Miguel de Melo, Madhava Krishna, Liam Paull, Florian Shkurti, and Antonio Torralba. Conceptfusion: Open-set multimodal 3d mapping, 2023. 1

[24] Olaf Kähler, Victor Adrian Prisacariu, Carl Yuheng Ren, Xin Sun, Philip H. S. Torr, and David William Murray. Very high frame rate volumetric integration of depth images on mobile devices. *IEEE Trans. Vis. Comput. Graph.*, 21(11): 1241–1250, 2015. 2

[25] Olaf Kähler, Victor A Prisacariu, and David W Murray. Real-time large-scale dense 3d reconstruction with loop closure. In *Computer Vision–ECCV 2016: 14th European Conference, Amsterdam, The Netherlands, October 11-14, 2016, Proceedings, Part VIII 14*, pages 500–516. Springer, 2016. 2

[26] Nikhil Keetha, Jay Karhade, Krishna Murthy Jatavallabhula, Gengshan Yang, Sebastian Scherer, Deva Ramanan, and Jonathon Luiten. Splatam: Splat, track and map 3d gaussians for dense rgb-d slam. In *Proceedings of the IEEE/CVF*

Conference on Computer Vision and Pattern Recognition, 2024. 2

[27] Maik Keller, Damien Lefloch, Martin Lambers, Shahram Izadi, Tim Weyrich, and Andreas Kolb. Real-time 3d reconstruction in dynamic scenes using point-based fusion. In *International Conference on 3D Vision (3DV)*, pages 1–8. IEEE, 2013. 1

[28] Bernhard Kerbl, Georgios Kopanas, Thomas Leimkühler, and George Drettakis. 3d gaussian splatting for real-time radiance field rendering. *ACM Transactions on Graphics*, 42(4), 2023. 13

[29] Bernhard Kerbl, Georgios Kopanas, Thomas Leimkühler, and George Drettakis. 3d gaussian splatting for real-time radiance field rendering. *ACM Transactions on Graphics*, 42(4), 2023. 1, 2

[30] Christian Kerl, Jürgen Sturm, and Daniel Cremers. Dense visual slam for rgb-d cameras. In *2013 IEEE/RSJ International Conference on Intelligent Robots and Systems*, pages 2100–2106. IEEE, 2013. 2

[31] Byeonghyeon Lee, Howoong Lee, Xiangyu Sun, Usman Ali, and Eunbyung Park. Deblurring 3d gaussian splatting. *arXiv preprint arXiv:2401.00834*, 2024. 2

[32] Kejie Li, Yansong Tang, Victor Adrian Prisacariu, and Philip HS Torr. Bnv-fusion: Dense 3d reconstruction using bi-level neural volume fusion. In *IEEE/CVF Conference on Computer Vision and Pattern Recognition*, pages 6166–6175, 2022. 1

[33] Lorenzo Liso, Erik Sandström, Vladimir Yugay, Luc Van Gool, and Martin R Oswald. Loopy-slam: Dense neural slam with loop closures. *arXiv preprint arXiv:2402.09944*, 2024. 2

[34] Peidong Liu, Xingxing Zuo, Viktor Larsson, and Marc Pollefeys. Mba-vo: Motion blur aware visual odometry. In *Proceedings of the IEEE/CVF International Conference on Computer Vision*, pages 5550–5559, 2021. 3

[35] Li Ma, Xiaoyu Li, Jing Liao, Qi Zhang, Xuan Wang, Jue Wang, and Pedro V Sander. Deblur-nerf: Neural radiance fields from blurry images. In *Proceedings of the IEEE/CVF Conference on Computer Vision and Pattern Recognition*, pages 12861–12870, 2022. 2

[36] Robert Maier, Jürgen Sturm, and Daniel Cremers. Submap-based bundle adjustment for 3d reconstruction from rgb-d data. In *Pattern Recognition: 36th German Conference, GCPR 2014, Münster, Germany, September 2-5, 2014, Proceedings 36*, pages 54–65. Springer, 2014. 2

[37] R Maier, R Schaller, and D Cremers. Efficient online surface correction for real-time large-scale 3d reconstruction. arxiv 2017. *arXiv preprint arXiv:1709.03763*, 2017. 2

[38] Yunxuan Mao, Xuan Yu, Kai Wang, Yue Wang, Rong Xiong, and Yiyi Liao. Ngel-slam: Neural implicit representation-based global consistent low-latency slam system. *arXiv preprint arXiv:2311.09525*, 2023. 2

[39] Hidenobu Matsuki, Edgar Sucar, Tristan Laidow, Kentaro Wada, Raluca Scona, and Andrew J Davison. imode: Real-time incremental monocular dense mapping using neural field. In *2023 IEEE International Conference on Robotics and Automation (ICRA)*, pages 4171–4177. IEEE, 2023. 1

[40] Hidenobu Matsuki, Keisuke Tateno, Michael Niemeyer, and Federic Tombari. Newton: Neural view-centric mapping for on-the-fly large-scale slam. *arXiv preprint arXiv:2303.13654*, 2023. 1, 2

[41] Hidenobu Matsuki, Riku Murai, Paul HJ Kelly, and Andrew J Davison. Gaussian splatting slam. In *Proceedings of the IEEE/CVF Conference on Computer Vision and Pattern Recognition*, pages 18039–18048, 2024. 2, 4, 5, 7, 8, 13, 14

[42] Ben Mildenhall, Pratul P. Srinivasan, Matthew Tancik, Jonathan T. Barron, Ravi Ramamoorthi, and Ren Ng. NeRF: Representing Scenes as Neural Radiance Fields for View Synthesis. In *European Conference on Computer Vision (ECCV)*. CVF, 2020. 1

[43] Thomas Müller, Alex Evans, Christoph Schied, and Alexander Keller. Instant neural graphics primitives with a multiresolution hash encoding. *arXiv preprint arXiv:2201.05989*, 2022. 1

[44] Richard A Newcombe, Shahram Izadi, Otmar Hilliges, David Molyneaux, David Kim, Andrew J Davison, Pushmeet Kohli, Jamie Shotton, Steve Hodges, and Andrew W Fitzgibbon. Kinectfusion: Real-time dense surface mapping and tracking. In *ISMAR*, pages 127–136, 2011. 1, 2

[45] Joseph Ortiz, Alexander Clegg, Jing Dong, Edgar Sucar, David Novotny, Michael Zollhoefer, and Mustafa Mukadam. isdf: Real-time neural signed distance fields for robot perception. *arXiv preprint arXiv:2204.02296*, 2022. 1, 2

[46] René Ranftl, Katrin Lasinger, David Hafner, Konrad Schindler, and Vladlen Koltun. Towards robust monocular depth estimation: Mixing datasets for zero-shot cross-dataset transfer. *IEEE Transactions on Pattern Analysis and Machine Intelligence (TPAMI)*, 2020. 6

[47] René Ranftl, Alexey Bochkovskiy, and Vladlen Koltun. Vision transformers for dense prediction. *ArXiv preprint*, 2021. 6

[48] Victor Reijgwart, Alexander Millane, Helen Oleynikova, Roland Siegwart, Cesar Cadena, and Juan Nieto. Voxgraph: Globally consistent, volumetric mapping using signed distance function submaps. *IEEE Robotics and Automation Letters*, 5(1):227–234, 2019. 2

[49] Antoni Rosinol, John J. Leonard, and Luca Carlone. NeRF-SLAM: Real-Time Dense Monocular SLAM with Neural Radiance Fields. *arXiv*, 2022. 1

[50] Denys Rozumnyi, Martin R. Oswald, Vittorio Ferrari, and Marc Pollefeys. Shape from blur: Recovering textured 3d shape and motion of fast moving objects. In *NeurIPS*, 2021. 2

[51] Denys Rozumnyi, Martin R. Oswald, Vittorio Ferrari, and Marc Pollefeys. Motion-from-blur: 3d shape and motion estimation of motion-blurred objects in videos. In *CVPR*, 2022. 2

[52] Erik Sandström, Yue Li, Luc Van Gool, and Martin R Oswald. Point-slam: Dense neural point cloud-based slam. In *International Conference on Computer Vision (ICCV)*. IEEE/CVF, 2023. 2

[53] Erik Sandström, Keisuke Tateno, Michael Oechsle, Michael Niemeyer, Luc Van Gool, Martin R Oswald, and Federico Tombari. Splat-slam: Globally optimized rgb-only slam with

3d gaussians. *arXiv preprint arXiv:2405.16544*, 2024. 2, 3, 4, 5, 6, 7, 8, 13, 14

[54] Erik Sandström, Kevin Ta, Luc Van Gool, and Martin R. Oswald. Uncle-SLAM: Uncertainty learning for dense neural SLAM. In *International Conference on Computer Vision Workshops (ICCVW)*, 2023. 1

[55] Thomas Schöps, Torsten Sattler, and Marc Pollefeys. BAD SLAM: Bundle adjusted direct RGB-D SLAM. In *Conference on Computer Vision and Pattern Recognition (CVPR)*, 2019. 7, 8

[56] Thomas Schops, Torsten Sattler, and Marc Pollefeys. BAD SLAM: Bundle adjusted direct RGB-D SLAM. In *CVF/IEEE Conference on Computer Vision and Pattern Recognition (CVPR)*, 2019. 1, 2

[57] Otto Seiskari, Jerry Ylilammi, Valtteri Kaatrasalo, Pekka Rantalankila, Matias Turkulainen, Juho Kannala, Esa Rahtu, and Arno Solin. Gaussian splatting on the move: Blur and rolling shutter compensation for natural camera motion, 2024. 2

[58] Nur Muhammad Mahi Shafiullah, Chris Paxton, Lerrel Pinto, Soumith Chintala, and Arthur Szlam. Clip-fields: Weakly supervised semantic fields for robotic memory, 2023. 2

[59] William Shen, Ge Yang, Alan Yu, Jansen Wong, Leslie Pack Kaelbling, and Phillip Isola. Distilled feature fields enable few-shot language-guided manipulation, 2023. 1

[60] Julian Straub, Thomas Whelan, Lingni Ma, Yufan Chen, Erik Wijmans, Simon Green, Jakob J Engel, Raul Mur-Artal, Carl Ren, Shobhit Verma, et al. The replica dataset: A digital replica of indoor spaces. *arXiv preprint arXiv:1906.05797*, 2019. 5, 6, 7, 13, 14

[61] Jörg Stückler and Sven Behnke. Multi-resolution surfel maps for efficient dense 3d modeling and tracking. *Journal of Visual Communication and Image Representation*, 25(1):137–147, 2014. 2

[62] Jürgen Sturm, Nikolas Engelhard, Felix Endres, Wolfram Burgard, and Daniel Cremers. A benchmark for the evaluation of rgb-d slam systems. In *2012 IEEE/RSJ international conference on intelligent robots and systems*, pages 573–580. IEEE, 2012. 7, 8, 13, 14

[63] Edgar Sucar, Shikun Liu, Joseph Ortiz, and Andrew J. Davison. iMAP: Implicit Mapping and Positioning in Real-Time. In *International Conference on Computer Vision (ICCV)*. IEEE/CVF, 2021. 1, 2

[64] Jiaming Sun, Yiming Xie, Linghao Chen, Xiaowei Zhou, and Hujun Bao. Neuralrecon: Real-time coherent 3d reconstruction from monocular video. In *IEEE/CVF Conference on Computer Vision and Pattern Recognition*, pages 15598–15607, 2021. 1

[65] Andrew Szot, Alex Clegg, Eric Undersander, Erik Wijmans, Yili Zhao, John Turner, Noah Maestre, Mustafa Mukadam, Devendra Chaplot, Oleksandr Maksymets, Aaron Gokaslan, Vladimir Vondrus, Sameer Dharur, Franziska Meier, Wojciech Galuba, Angel Chang, Zsolt Kira, Vladlen Koltun, Jitendra Malik, Manolis Savva, and Dhruv Batra. Habitat 2.0: Training home assistants to rearrange their habitat. In *Advances in Neural Information Processing Systems (NeurIPS)*, 2021. 7

[66] Chengzhou Tang and Ping Tan. Ba-net: Dense bundle adjustment network. *ArXiv*, abs/1806.04807, 2018. 5

[67] Yijie Tang, Jiazhao Zhang, Zhinan Yu, He Wang, and Kai Xu. Mips-fusion: Multi-implicit-submaps for scalable and robust online neural rgb-d reconstruction. *arXiv preprint arXiv:2308.08741*, 2023. 2

[68] Zachary Teed and Jia Deng. Droid-slam: Deep visual slam for monocular, stereo, and rgb-d cameras. *Advances in neural information processing systems*, 34:16558–16569, 2021. 1, 2, 5

[69] Fabio Tosi, Youmin Zhang, Ziren Gong, Erik Sandström, Stefano Mattoccia, Martin R. Oswald, and Matteo Poggi. How nerfs and 3d gaussian splatting are reshaping slam: a survey, 2024. 2

[70] Hao Wang, Jun Wang, and Wang Liang. Online reconstruction of indoor scenes from rgb-d streams. In *Proceedings of the IEEE Conference on Computer Vision and Pattern Recognition*, pages 3271–3279, 2016. 2

[71] Hengyi Wang, Jingwen Wang, and Lourdes Agapito. Coslam: Joint coordinate and sparse parametric encodings for neural real-time slam, 2023. 2

[72] Peng Wang, Lingzhe Zhao, Ruijie Ma, and Peidong Liu. Badnerf: Bundle adjusted deblur neural radiance fields. In *Proceedings of the IEEE/CVF Conference on Computer Vision and Pattern Recognition*, pages 4170–4179, 2023. 2, 3

[73] Zhou Wang, Alan C Bovik, Hamid R Sheikh, and Eero P Simoncelli. Image quality assessment: from error visibility to structural similarity. *IEEE transactions on image processing*, 13(4):600–612, 2004. 7

[74] Silvan Weder, Johannes Schonberger, Marc Pollefeys, and Martin R Oswald. Routedfusion: Learning real-time depth map fusion. In *IEEE/CVF Conference on Computer Vision and Pattern Recognition*, pages 4887–4897, 2020. 1

[75] Silvan Weder, Johannes L Schonberger, Marc Pollefeys, and Martin R Oswald. Neuralfusion: Online depth fusion in latent space. In *IEEE/CVF Conference on Computer Vision and Pattern Recognition*, pages 3162–3172, 2021. 1

[76] Chi Yan, Delin Qu, Dong Wang, Dan Xu, Zhigang Wang, Bin Zhao, and Xuelong Li. Gs-slam: Dense visual slam with 3d gaussian splatting. *arXiv preprint arXiv:2311.11700*, 2023. 2

[77] Zhixin Yan, Mao Ye, and Liu Ren. Dense visual slam with probabilistic surfel map. *IEEE transactions on visualization and computer graphics*, 23(11):2389–2398, 2017. 2

[78] Lihe Yang, Bingyi Kang, Zilong Huang, Zhen Zhao, Xiaogang Xu, Jiashi Feng, and Hengshuang Zhao. Depth anything v2. *arXiv preprint arXiv:2406.09414*, 2024. 13

[79] Xingrui Yang, Hai Li, Hongjia Zhai, Yuhang Ming, Yuqian Liu, and Guofeng Zhang. Vox-fusion: Dense tracking and mapping with voxel-based neural implicit representation. In *IEEE International Symposium on Mixed and Augmented Reality (ISMAR)*, pages 499–507. IEEE, 2022. 1

[80] Xingrui Yang, Yuhang Ming, Zhaopeng Cui, and Andrew Calway. Fd-slam: 3-d reconstruction using features and dense matching. In *2022 International Conference on Robotics and Automation (ICRA)*, pages 8040–8046. IEEE, 2022. 2

[81] Vladimir Yugay, Yue Li, Theo Gevers, and Martin R. Oswald. Gaussian-slam: Photo-realistic dense slam with gaussian splatting, 2023. 2

[82] Ganlin Zhang, Erik Sandström, Youmin Zhang, Manthan Patel, Luc Van Gool, and Martin R. Oswald. Glorie-slam: Globally optimized rgb-only implicit encoding point cloud slam, 2024. 2, 5, 13

[83] Richard Zhang, Phillip Isola, Alexei A Efros, Eli Shechtman, and Oliver Wang. The unreasonable effectiveness of deep features as a perceptual metric. In *Proceedings of the IEEE conference on computer vision and pattern recognition*, pages 586–595, 2018. 7

[84] Wei Zhang, Tiecheng Sun, Sen Wang, Qing Cheng, and Norbert Haala. Hi-slam: Monocular real-time dense mapping with hybrid implicit fields. *IEEE Robotics and Automation Letters*, 2023. 2

[85] Wei Zhang, Tiecheng Sun, Sen Wang, Qing Cheng, and Norbert Haala. Hi-slam: Monocular real-time dense mapping with hybrid implicit fields, 2023. 1, 2

[86] Youmin Zhang, Fabio Tosi, Stefano Mattoccia, and Matteo Poggi. Go-slam: Global optimization for consistent 3d instant reconstruction. In *Proceedings of the IEEE/CVF International Conference on Computer Vision*, pages 3727–3737, 2023. 1, 2

[87] Lingzhe Zhao, Peng Wang, and Peidong Liu. Bad-gaussians: Bundle adjusted deblur gaussian splatting. In *European Conference on Computer Vision*, pages 233–250. Springer, 2025. 2, 3

[88] Yiming Zhao, Denys Rozumnyi, Jie Song, Otmar Hilliges, Marc Pollefeys, and Martin R. Oswald. Human from blur: Human pose tracking from blurry images. In *Proceedings of the IEEE/CVF International Conference on Computer Vision (ICCV)*, pages 14905–14915, 2023. 2

[89] Zihan Zhu, Songyou Peng, Viktor Larsson, Weiwei Xu, Hujun Bao, Zhaopeng Cui, Martin R Oswald, and Marc Pollefeys. Nice-slam: Neural implicit scalable encoding for slam. In *IEEE/CVF Conference on Computer Vision and Pattern Recognition*, pages 12786–12796, 2022. 1

[90] Zi-Xin Zou, Shi-Sheng Huang, Yan-Pei Cao, Tai-Jiang Mu, Ying Shan, and Hongbo Fu. Mononeuralfusion: Online monocular neural 3d reconstruction with geometric priors. *arXiv preprint arXiv:2209.15153*, 2022. 1

[91] Matthias Zwicker, Hanspeter Pfister, Jeroen Van Baar, and Markus Gross. Surface splatting. In *Proceedings of the 28th annual conference on Computer graphics and interactive techniques*, pages 371–378, 2001. 4

Deblur Gaussian Splatting SLAM

Supplementary Material

6. Method Details

Hyperparameters. We use 150 iterations for mapping and 200 iterations for the frame-to-model tracking. We set $\lambda = 0.8$, $\lambda_{SSIM} = 0.2$, $\lambda_{reg} = 10$. The learning rate for the rotational relative pose is set to $3e-3$ and $1e-3$. We keep the early stopping in the frame-to-model tracking when the gradient goes under $1e-4$, as introduced in [41] for faster tracking. For the other hyperparameters please refer to [41, 53, 82]

Keyframes Management. We use the keyframe window as in MonoGS [41]. The keyframe selection is based on the covisibility of the Gaussians. The covisibility between two keyframes i, j, is defined using the Intersection over Union (IoU) and Overlap Coefficient (OC):

$$\text{IoU}_{\text{cov}}(i,j) = \frac{|\mathcal{G}_v^i \cap \mathcal{G}_v^j|}{|\mathcal{G}_v^i \cup \mathcal{G}_v^j|}, \tag{18}$$

$$\text{OC}_{\text{cov}}(i,j) = \frac{|\mathcal{G}_v^i \cap \mathcal{G}_v^j|}{\min(|\mathcal{G}_v^i|, |\mathcal{G}_v^j|)}, \tag{19}$$

where $\mathcal{G}_v^i$ are the Gaussians visible in keyframe i. A Gaussian is defined visible in a rasterization if the ray's accumulated transmittance α has not yet reached 0.5.

A keyframe i is added to the keyframe window KFs if, given the last keyframe j, $\text{IoU}_{\text{cov}}(i,j) < k_{\text{fcov}}$ or if the relative translation $t_{ij} > k_{fm}\hat{D}_i$, where $\hat{D}_i$ is the median depth of the mid pose of frame i. For Replica we use $k_{\text{fcov}} = 0.95$, $k_{\text{fm}} = 0.04$ and for TUM-RGBD [62] and ScanNet [10] datasets, $k_{\text{fcov}} = 0.90$, $k_{\text{fm}} = 0.08$. The registered keyframe j in KFs is removed if $\text{OC}_{\text{cov}}(i,j) < k_{\text{fc}}$, where keyframe i is the latest added keyframe. For all datasets, the cutoff is set to $k_{\text{fc}} = 0.3$. The size of the keyframe window is set to $|\text{KFs}| = 10$ for Replica and $|\text{KFs}| = 8$ for TUM-RGBD and ScanNet.

Pruning and Densification. The Pruning and Densification are done similarly to MonoGS [41]. Pruning in the system is guided by visibility criteria. Newly inserted Gaussians from the last three keyframes are discarded if they are not observed by at least three other frames within the keyframe window, but this process only occurs when the keyframe window reaches its capacity. Additionally, for every 150 mapping iterations, a global pruning step removes Gaussians with opacity below 0.7 or those with excessively large 2D projections. Densification follows the method outlined in [28] and is similarly performed every 150 mapping iteration. To avoid forgetting Gaussian, while mapping the current window, we select a few indices of past keyframes and add

Method	Metric	office0
Deblur-SLAM **(DepthAnything V2 [78])**	sPSNR↑ sSSIM↑ sLPIPS↓	30.06 0.87 0.25
Deblur-SLAM **(Omnidepth [14])**	sPSNR↑ sSSIM↑ sLPIPS↓	**30.40** **0.87** **0.24**

Table 6. **Monocular Depth Estimator evaluation on Replica [60].** The results are almost equal, showing that there is not much difference between the two Monocular Depth Estimators. We selected OmniDepth [14] being the most consistent, even in blurry frames.

them to the mapping optimization to preserve rendering quality and geometry on the whole scene.

Refinement. Following the method outlined in [53], online global BA is conducted every 20 keyframes. We perform both the GlORIE-SLAM [82] trajectory refinement and MonoGS [41] color refinement at the end of the online optimization. We keep 26000 as the number of refinement optimizations as in MonoGS.

Monocular Depth Estimator. We used OmniDepth [14] as a Monocular Depth Estimator as employed in [53] to fill the depth map where the multi-view is invalid. We have tried Depth Anything v2 [78], but in our blurry setting, we found OmniDepth to be more robust (Table 6).

Details on the Scale and Shift estimation. Following [53], the scale θ_i and shift γ_i are initially estimated using least squares fitting using:

$$\{\theta_i, \gamma_i\} = \arg\min_{\theta, \gamma} \sum_{(u,v)} \left((\theta(1/D_i^{\text{mono}}) + \gamma) - d_i^l \right)^2 \tag{20}$$

Disparity Maps Details. For a given disparity map d_i (separated into low and high error parts $\{d_i^l, d_i^h\}$) for frame i, we denote the corresponding depth $\tilde{D}_i = 1/d_i$. Similar to [53], pixel correspondences (u, v) and $(\hat{u}, \hat{v})$ between keyframes i and j are established by warping (u, v) into frame j with depth $\tilde{D}_i$ as

$$p_i = \omega_i \tilde{D}_i(u,v) K^{-1}[u,v,1]^T, \quad [\hat{u}, \hat{v}, 1]^T \propto K\omega_j^{-1}[p_i, 1]^T \tag{21}$$

The 3D point corresponding to $(\hat{u}, \hat{v})$ is computed from the depth at $(\hat{u}, \hat{v})$ as

$$p_j = \omega_j \tilde{D}_j(\hat{u}, \hat{v}) K^{-1}[\hat{u}, \hat{v}, 1]^T \tag{22}$$

If the L2 distance between p_i and p_j is smaller than a threshold, the depth $\tilde{D}_i(u,v)$ is consistent between i and j. By looping over all keyframes except i, the global two-view

Figure 6. **Qualitative results on averaged real-world TUM-RGBD data (`f2/xyz`) [62]**, in which we averaged 5 frames. Given the blurry input frames, we can track the trajectory with sub-frame precision and estimate sharp maps by directly modeling the camera motion blur.

Method	Metric	$M = 3$	$M = 6$	$M = 9$
Deblur-SLAM (Ours)	sPSNR↑	28.90	30.11	**30.40**
	sSSIM↑	0.85	0.87	**0.87**
	sLPIPS↓	0.29	0.25	**0.24**

Table 7. **Ablation on the number of virtual cameras on `office0` [60].** We observe that the rendering metrics increase with the number of virtual cameras used. This indicates that more virtual cams make the blur modeling more accurate and lead to sharp renderings.

consistency n_i can be computed for frame i as

$$n_i(u, v) = \sum_{k \in \text{KFs}, k \neq i} \mathbb{1}\left(\|p_i - p_k\|_2 < \eta \cdot \text{avg}\left(\tilde{D}_i\right)\right) \quad (23)$$

Here, $\mathbb{1}(.)$ is the indicator function, $\eta \in \mathbb{R}_{\geq 0}$ is a hyperparameter, and n_i is the total two-view consistency for pixel (u, v) in keyframe i. Moreover, $\tilde{D}_i(u, v)$ is valid if n_i is larger than a threshold.

7. Additional Experimental Results

Effect on the number of virtual views. We analyze the impact of varying the number of virtual cameras in `office0` to evaluate its influence on the rendering performance. As shown in Table 7, our results reveal that an increasing the number of virtual cameras consistently improves rendering quality. This highlights the significance of optimizing the number of virtual cameras to enhance the overall performance of the system.

Ablation on features. In our study, we conducted a comprehensive ablation analysis on key components of our model to demonstrate their individual contributions to overall performance. The results, detailed in Table 8, clearly indicate that our full method, incorporating physical blur modeling, frame-to-frame tracking, Gaussian deformations, and final refinement, surpasses all variants lacking one or more of these elements in rendering quality. This emphasizes the integral role each component plays in enhancing our method's rendering capabilities, validating our approach of integrating these techniques for optimal results.

Test on Blurry Real-World Dataset. We averaged 5 frames for the TUM-RGBD dataset and 2 frames for the

Method	Physical Blur Model	Frame-to-Frame	Gaussian Deformation	Refine-ment	Metric	office0
MonoGS [41]	✗	✗	✗	✓	sPSNR↑	25.30
					sSSIM↑	0.82
					sLPIPS↓	0.43
MonoGS + Deblurring	✓	✗	✗	✗	sPSNR↑	25.91
					sSSIM↑	0.83
					sLPIPS↓	0.40
Deblur-SLAM No Deformation No Refinement	✓	✓	✗	✗	sPSNR↑	28.23
					sSSIM↑	0.84
					sLPIPS↓	0.33
Deblur-SLAM (Ours)	✓	✓	✓	✓	sPSNR↑	**30.40**
					sSSIM↑	**0.87**
					sLPIPS↓	**0.24**

Table 8. **Ablation on the different features of our method on `office0` [60].** This table showcases the individual contributions of various features in our method, demonstrating how each component enhances overall performance and justifying our design choice.

Method	Metric	Avg 3fr	Avg 5fr	Avg 7fr
SplatSLAM [53]	PSNR↑	**27.64**	**27.32**	**27.11**
	SSIM↑	0.88	0.87	**0.88**
	LPIPS↓	0.14	0.17	**0.17**
	sPSNR↑	20.44	17.61	20.18
	sSSIM↑	0.68	0.59	0.66
	sLPIPS↓	0.22	0.30	0.30
	ATE↓	21.8	21.8	21.8
Deblur-SLAM (Ours)	PSNR↑	27.26	27.00	25.90
	SSIM↑	**0.90**	**0.89**	0.87
	LPIPS↓	**0.11**	**0.14**	**0.17**
	sPSNR↑	**20.70**	**20.70**	**20.37**
	sSSIM↑	**0.70**	**0.70**	**0.68**
	sLPIPS↓	**0.18**	**0.21**	**0.26**
	ATE↓	**0.2**	**0.2**	**0.2**

Table 9. **Rendering evaluation on custom `f2/xyz` [62] with averaged frames.** By averaging some frames to introduce blur, we show that our method outperforms others in rendering metrics for sharp images (denoted with the "s" prefix) as well as better ATE. Deblur-SLAM achieves comparable results for the averaged renderings metrics.

ETH3D dataset. On Table 9, we show that Deblur-SLAM can outperform almost all the metrics. More specifically, the better sPSNR, sSSIM, sLPIPS denote that our methods successfully learn a sharper map. An example result in comparison with SplatSlam [53] is depicted in Figure 6.

Method	Metric	106_00
Deblur-SLAM Light	FPS [frame/s]↑	**0.65**
	PSNR↑	22.90
Deblur-SLAM	FPS [frame/s]↑	0.36
	PSNR↑	**23.06**

Table 10. **Speed performances on ScanNet [10],** compared to a lighter version of our model with 120 iterations for mapping and 20 for frame-to-model tracking.